JP3J.10

TRADE WIND CUMULI STATISTICS AND THE IMPACT OF FINITE RESOLUTION MEASUREMENTS

Guangyu Zhao* and Larry Di Girolamo
University of Illinois at Urbana-Champaign

1. INTRODUCTION

Trade wind cumuli's crucial role in climate and global energy cycle has promoted numerous model studies that attempt to characterize the dynamic and radiative interactions between trade wind cumuli and their environment [see Zhao and Austin (2005) for a review]. Evaluating these cloud models requires quantitative information of cumuli macrophysical properties, which can be measured from ground-based, in situ, and satellite instruments. However, trade wind cumuli range from a few meters to a few kilometers in size making them difficult to detect by most meteorological satellites. Therefore, studies of this these clouds demand high-resolution satellite data.

We present a comprehensive statistical overview of cumulus cloud macrophysical properties over the Tropical Western Atlantic based on measurements taken by the Advanced Spaceborne Thermal Emission and Reflection Radiometer (ASTER). The results from our ASTER analyses show important deviations from previous work on the statistics of cumuli [see Benner and Curry (1998) for a review]. The impact of finite resolution measurement on cumuli statistics is also examined with data taken by ASTER and the Multiangle Imaging Spectral Radiometer (MISR).

2. ASTER DATA

ASTER is on the EOS Terra, which is in a 705m sun synchronized orbit and crosses the equator at ~1030 local solar time. Details of the ASTER instrument and its performance can be found in Yamaguchi et al. (1998). In brief, ASTER has one nadir camera, which has three visible near-infrared (VIR) spectral bands (0.5 to 1.0 μm) with 15 m spatial resolution, six shortwave infrared (SWIR) spectral bands (1.0 to 2.5 μm) with 30 m spatial resolution, and five thermal infrared (TIR) spectral bands (8 to 12 μm) with 90 m spatial resolution. ASTER produces about 650 scenes per day. Each scene has a spatial coverage of 60 x 60 km^2.

Although ASTER data are primarily collected over land, the instrument was tasked to acquire data over 20º – 12º N latitude, 66º-55º W longitude between September and December 2004 as part of the Rain In Cumulus over Ocean (RICO) experiments (http://www.joss.ucar.edu/rico). The ASTER data are Level 1B calibrated radiance data. Between Sep. and Dec., 448 scenes were collected on 38 days. Scenes contaminated any cirrus clouds are manually discarded by visual inspections. 138 scenes from 28 separate days remained containing small to large cumuli, and their property is given below.

Corresponding author address: Guangyu Zhao, Univ. of Illinois, Dept of Atmospheric Sciences, Urbana, IL 61801; e-mail: gyzhao@atmos.uiuc.edu

3. CLOUD MASKING AND LABELLING

A cloud mask classifies the satellite instantaneous fields of view (pixels) as either clear or cloudy. Although there are numerous cloud detection algorithms [see, e.g., Goodman and Henderson-Sellers (1988) for a review], a single threshold approach is appropriate for this study, given the variation of clear radiance throughout a scene is small and the radiative and spatial contrast between bright clouds and dark ocean is large. Channel 3N (0.78 ~ 0.8 μm) is chosen to minimize Raleigh scattering and water vapor absorption simultaneously. A pixel will be flagged cloudy if its digital number is larger than predetermined threshold manually chosen for each scene. Otherwise, it will be flagged as clear.

Once pixels are classified as either clear or cloudy, they are grouped into individual clouds. Two cloudy pixels belong to the same cloud if they share one edge. For the 138 scenes, the total number of the clouds is 935,5344, which is one or two orders magnitude larger than previous studies.

4. SATISTICS

4.1 Cloud Cover Density

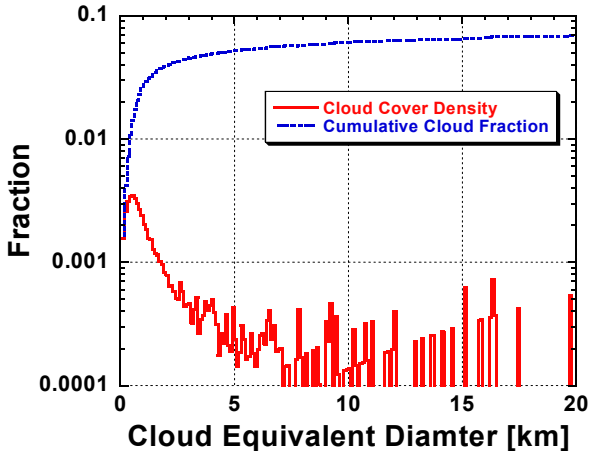

Figure 1. Cloud fraction as a function of cloud equivalent diameter. The dashed line represents cumulative cloud fraction and the solid line represents cloud cover density.

Figure 1 shows the cloud cover density, defined as the cloud cover percentage of all the clouds within a certain size range. The dominant cloud fraction is 500m. In past studies, the dominant cloud fraction ranges from 100m to 1km. The total cloud fraction is approximately 7%, and half of the cloud fraction is from clouds smaller than 1.5 km. Notice the cloud cover density curve becomes less smooth when the cloud size becomes larger because of fewer samples of larger clouds.

4.2 Cloud Size Distribution

The cloud size distribution is defined as the probability of occurrence of clouds having a certain size range. Recent studies show that the size distribution can be best represented as a power law of the form: $n(D) = aD^{-b}$, where D is the cloud area-equivalent diameter. Past studies show that b ranges from 0.48 to 3.6 with and without a scale break. However, the existence of the scale break is believed to be true in recent studies and has been used to validate models against observations.

Figure 2 shows the normalized histogram of all the clouds binned at the 100 m diameter increments in logarithmic coordinates. A 100m bin width is the smallest bin used in past studies. The exponent b determined from the slope of the line fit, is 2.99 and the correlation coefficient (R) of the fitting is 0.9998. Notice the absence of a scale break. However, if all the clouds are stratified into 28 separate dates and a histogram is drawn for each day, a scale break may appear for some days when the number of clouds is small.

4.3 Area-Perimeter Realtionship

Lovejoy (1982) first reporteded clouds obey the following area-perimeter relationship:

$$P \approx \sqrt{A^d}$$

where A is the area, P is the perimeter, and d is the fractal dimension. d characterizes the degree of complexity of cloud shape. For regular shapes (i.e., square and circle), d = 1. Greater d means that cloud shapes are more contorted. It is believed that the value of d is rooted in turbulent theory and has been used as a critical test for cloud resolving models. For cumulus clouds, d is approximately 4/3 in the past studies.

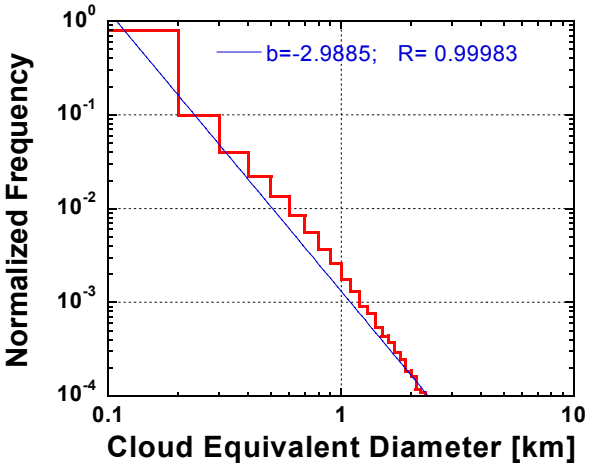

Figure 2. The histogram of cloud size distribution with 100m bin width.

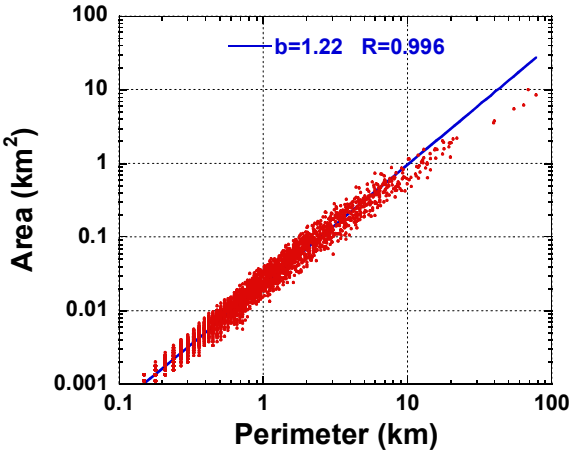

Figure 3. The scatter plot of cloud area versus cloud perimeter.

Figure 3 gives the log-log scatter plot of cloud perimeter versus cloud area. The perimeter of each cloud is the total length of all the edges adjacent to non-cloudy pixels. Cloud area is the product of the number of cloudy pixels and the size of each pixel. The fractal dimension, d, is 1.22 and the correlation coefficient is 0.996. d is much smaller than 4/3, indicating that cumulus clouds have less contorted shapes than pervious results.

4.4 Cloud Top Height Distribution

With ASTER TIR 12μm data, the cloud top height for each 90m pixel is retrieved by inversing the radiance into the brightness temperature (BT) and then relating BT with the temperature profile from the nearby

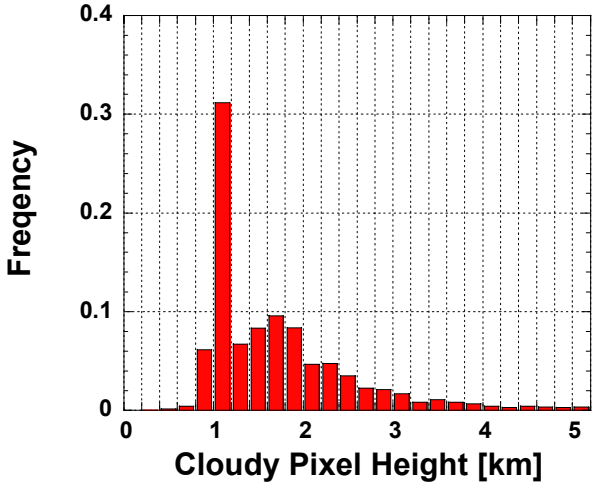

Figure 4. The histogram of cloudy pixel height at 90m resolution.

soundings. The cloud top height for each 90m pixel is retrieved only if all the 15m resolution pixels within it are flagged as cloudy by the corresponding 15m cloud mask. Although water vapor absorption is not corrected, the biases in cloud top heights are believed to be less than 200m based on the radiative model simulations. Figure 4 shows the cloud top height histogram with a peak around 1km. The bimodality needs further investigation.

5. RESOLUTION EFFECT

The dependency of cloud fraction on the pixel resolution is also examined. As shown in Fig. 5, cloud fraction will slightly increase as instrument resolution decreases under the assumption that threshold is set perfectly for high-resolution data and fixed during the degrading process. An analogous experiment was done by Wielicki and Welch (1986), who tested the sensitivity of cloud fraction to spatial resolution. However, the usage of the resulting cloud masks generates biases both in cloud climatology and aerosol retrievals.

Ideally, a cloud mask should flag pixels containing even a small amount of cloud (e.g. for the purpose of aerosol retrieval). However, the cloud fraction calculated from such an ideal cloud mask would be larger than the true cloud fraction. This is illustrated in Fig. 6 and in accordance with the theoretical study by Di Girolamo and Davis (1997). Comparing cloud fractions from the 1.1km ideal cloud masks with cloud fractions from the 1.1km MISR cloud mask shows the MISR cloud mask is doing an excellent job in detecting cumulus clouds.

6. FUTURE WORK

One important factor, which may highly impact the statistics and has not been considered in the current study, is the meteorological conditions such as wind, sea surface temperature, and lifting condensation level. In the near future, we will stratify all the statistics by different meteorological conditions. We will also examine how the statistics vary with different measurements from different satellite instruments and try to quantify the biases in aerosol retrieval due to cloud contaminations.

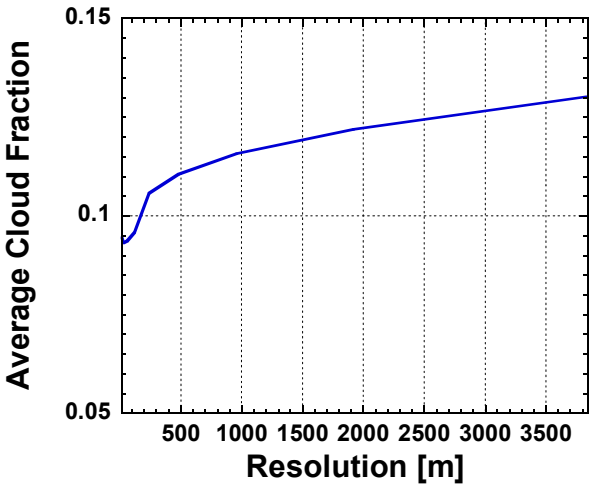

Figure 5. The average cloud fraction for the 138 cloud masks as a function of resolution keeping the same threshold used in 15m cloud mask and applied to the degraded radiance field.

Acknowledgements. The research is supported by RICO and MISR grants. We thank Dr. Bob Rauber for useful discussions and Eric Snodgrass for the assistance of acquiring ASTER data.

REFERENCES

Benner T.C. and J.A. Curry, 1998: Characteristics of small tropical cumulus clouds and their impact on the environment . *J. Geophys. Res.,* **103**, 28753-28767.

Di Girolamo L. and Davis R., 1997: Cloud fraction errors caused by finite resolution measurements. *J. Geophys. Res.,* **102**, 1739-1756.

Goodman, A.H., and A. Henderson-Sellers, 1988: Cloud detection and analysis: A review of recent progress. *Atmos. Res*., **21**, 203-228.

Lovejoy S., 1982:Area-Perimeter Relation for Rain and Cloud Areas. *Science*, **216**,185-187.

Wielicki B.A., and R.M. Welch, 1986: Cumulus cloud properties derived using LANDSAT data. *J. Climate Appl. Meteor.*, **25**, 261-276.

Yamaguchi Y., A.B. Kahle, H. Tsu , T. Kawakami, and M. Pniel, 1998: Overview of Advanced Spaceborne Thermal Emission and Reflection Radiometer (ASTER). *IEEE Trans. Geosci. Remote Sens.*, **36**, 1062-1071.

Zhao M. and Austin P.H., 2005: Life cycle of numerically simulated shallow cumulus clouds. Part I: Transport. *J. Atmos. Sci*., **62**, 1269-1290.

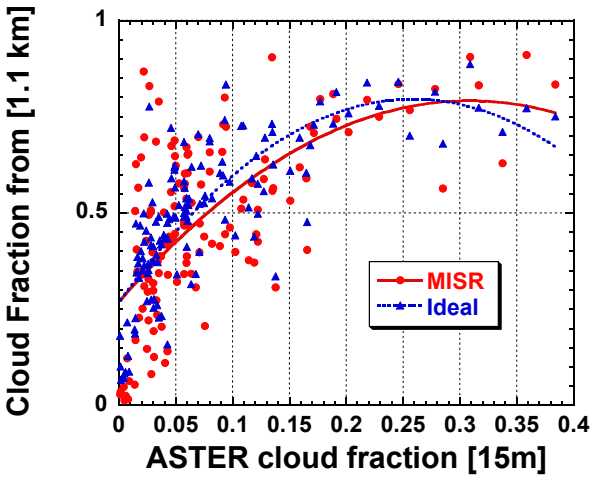

Figure 6. The scatter plot of cloud fractions from cloud fractions from 1.1km MISR cloud masks and ideal cloud masks for all 138 scenes versus 15m ASTER cloud masks. The 1.1km ideal cloud masks are generated by flagging as cloudy any 1.1 pixel that contains some 15m cloudy pixels based on 15m ASTER cloud mask.